Airborne estimation of SO_2 emissions rates from a coal-fired power plant using two top-down methods: A mass balance model and Gaussian footprint approach

Jeonghwan Kim [a], Beom-keun Seo [a,b], Taehyoung Lee [a], Jongho Kim [c], Saewung Kim [d], Gwi-Nam Bae [e], Gangwoong Lee [a,*]

[a] *Department of Environmental Sciences, Hankuk University of Foreign Studies, Yongin, South Korea*
[b] *Environmental Research Center, Hanseo University, Seosan, South Korea*
[c] *Department of Environmental Engineering, Graduate School of Hanseo University, Seosan, South Korea*
[d] *Department of Chemistry, University of California, Irvine, USA*
[e] *Center for FRIEND Project, Korea Institute of Science and Technology, Seoul, South Korea*
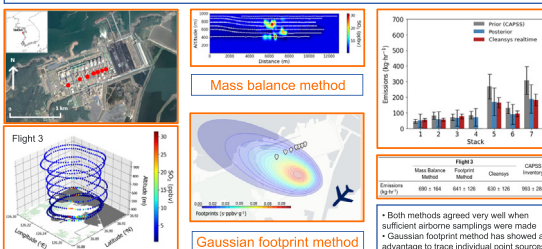
HIGHLIGHTS

- SO2 emissions rates from a point source were assessed by two top-down methods.
- Both methods agreed well when sufficient spatial sampling resolutions were made.
- Gaussian footprint method showed distinct advantage to trace individual point sources.
- Top-down SO2 emission estimation accuracy was enhanced by using both methods.

GRAPHICAL ABSTRACT

ARTICLE INFO

ABSTRACT

In this study, two top-down methods—mass balance and Gaussian footprint—were used to determine SO2 emissions rates via three airborne sampling studies over Korea's largest coal power plant in October 2019 and 2020. During the first two flights in October 2019, mass balance approaches significantly underestimated the SO2 emissions rates by 75 % and 28 %, respectively, as obtained from the real-time stack monitoring system. Notably, this large discrepancy accounted for the insufficient number of transects altitudes and high levels of background SO2 along the upwind side. Alternatively, the estimated SO2 emissions rates of the third flight (October 2020) displayed a difference of <10 % from rea-time monitoring data (630 vs. 690 kg·hr^{-1}), owing to the enhanced vertical resolution with increased transects and lower background SO2 levels. In contrast to the mass balance method, Gaussian footprints offered significantly improved accuracy (relative error: 41 %, 32 %, and 2 % for Flights 1, 2, and 3, respectively). This relatively good performance was attributed to prior emissions knowledge via the Clean Air Policy Support System (CAPSS) emissions inventory and its unique ability to accurately estimate stack-level SO2 emissions rates. Theoretically, the Gaussian footprint was less prone to sparse transects and upwind background levels. However, it can be substantially influenced by atmospheric stability and consequently by effective stack heights and dispersion parameters; basically, all factors with minimal-to-no influence on the mass balance approach. Conversely, the mass balance method was the only plausible approach to estimate unidentified source emissions rates when well-defined prior emission information

---

was unknown. Here, the footprint approach supplemented the mass balance method when the emission inventories were known, and employing both strategies approaches greatly enhanced the integrity of top-down emissions inventories from the power plant sources, thus, supporting their potential for ensuring operational compliance with SO_2 emissions regulation.

1. Introduction

Atmospheric SO_2 can cause adverse effects on both humans and ecosystems (Cape et al., 2003; Henschel et al., 2012). WHO (World Health Organization, 2021) has noted substantial excess mortalities above air quality guideline (AQG) concentrations of 40 μg·m^{-3} SO_2. Furthermore, recent studies have confirmed the health benefits of reducing SO_2 levels below AQGs (Orellano et al., 2021; Zheng et al., 2021), demonstrating a ~1 % increase in hospital admissions and 0.6–0.7 % increase in mortality per every 10 μg·m^{-3} increase in daily mean SO_2 levels above zero levels. Additionally, SO_2 is the primary precursor of sulfate aerosols, which significantly impact health and climate (Lelieveld and Heintzenberg, 1992; Park et al., 2018). Fortunately, ambient SO_2 emissions and concentrations in many parts of the world have decreased substantially due to compulsory regulations and technologies, primarily from large point sources, such as coal power plants (Kim and Yeo, 2013; Tang et al., 2020). As part of the verification and supervision process, reported SO_2 emissions inventories and compliance with legal regulations must be verified periodically by monitoring the major emissions sources.

Atmospheric SO_2 primarily originates from fossil fuel combustion, particularly that of coal and oil. Point sources from energy production, industrial, and manufacturing facilities are the predominant SO_2 emissions in Korea, accounting for 81 % of the 358 kt SO_2·yr^{-1} released (Choi et al., 2020). Specifically, power plant emissions account for the most significant proportion (31 %) of the point sources; accordingly, strict regulations have been placed by setting SO_2 emissions limits for each stack in all large-scale point sources. The emitted SO_2 concentrations and air flows from all stacks in selected point sources are measured continuously in real time and are collected by an online central server to ensure compliance (Choi and Jo, 2011). Currently, automatic telemonitoring systems are installed in 1477 stacks across 569 facilities in South Korea, and their real-time data can be accessed via Cleansys (https://cleansys.or.kr/index.do). Conventionally, the quality of hourly stack SO_2 monitoring data has been evaluated by performance reviews using side-by-side intercomparisons with a reference method every 2 years. However, this bottom-up approach is impractical due to the sheer number of stacks requiring periodic monitoring.

Alternatively, optical open-path remote sensing has been used to monitor emissions along facility boundaries and beyond (Sanchez et al., 2019; Smith, 2015). Although it is an excellent tool for monitoring fugitive emissions and leak detections of area sources, it is inadequate for observing elevated emissions from high-level point sources, such as stacks. Satellite measurements have also proven capable of monitoring sizeable SO_2 point sources (Carn et al., 2007; McLinden et al., 2012; Theys et al., 2015); however, these studies have successfully assessed anthropogenic SO_2 emissions over the long-term, while variations in short-term (hourly to daily) emissions rates (ERs) remain largely unexplored (Duncan et al., 2014).

Airborne measurements using a mass balance model represent one top-down approach for real-time estimation of ground emissions sources (Gordon et al., 2015). For example, Fried et al. (2020) estimated volatile organic compounds (VOCs) and SO_2 emissions from a petrochemical facility in Korea using DC-8 measurements, obtaining a strong agreement of SO_2 estimates between airborne top-down and bottom-up values. Additional SO_2 emission assessments from large point sources in facilities throughout Korea have been conducted using airborne observations (Kim et al., 2020; Park et al., 2020) by applying a similar mass balance model to calculate SO_2 emissions, successfully demonstrating the utility of this top-down approach at estimating point source emissions. Another top-down approach combines observations at receptors with a dispersion model via an inverse technique and has been widely used elsewhere to

estimate various emission inventories from local- to global scales (Ars et al., 2017; Brioude et al., 2011; Stohl et al., 2009; Vaughan et al., 2016). This inverse method is known to be more unstable to small changes in input parameters than other methods (Lushi and Stockie, 2010); thus, they have been widely employed for evaluating the emissions of conservative and inert species like halocarbons (Stohl et al., 2009). Alternatively, emissions estimates using this technique for reactive and aerosol species have focused on near-field point or area sources (Brioude et al., 2011; Cantelli et al., 2011; Hosseini and Stockie, 2016; Vaughan et al., 2016). For example, SO_2 emissions from point sources were tested using experimental field data across a flat grassland under different atmospheric stability conditions, revealing that the inverse technique with the Gaussian plume model produced reasonably well-defined SO_2 point-source emissions estimates given known source heights, locations, and nominal atmospheric conditions (Mao et al., 2022).

In the present study, two top-down approaches—mass balance and the Gaussian footprint method—were employed to estimate power plant SO_2 emissions using aircraft observations. The results of each approach were compared with real-time stack monitoring data, and implications were drawn regarding the feasibility of monitoring airborne SO_2 ERs for large-scale point sources. The accuracy and uncertainties in determining SO_2 ERs were identified for each model. The present study aimed to assess the advantages of multi-approach top-down estimation methods for minimizing the differences between emissions inventories and real-world data.

2. Methods

2.1. Taean power plant

The Taean power plant was selected for this analysis based on its well-established emissions inventories and real-time stack monitoring data availability. It is the largest operational coal-power plant in Korea and is located 100 km southwest of Seoul along the western coast of the Korean Peninsula (Fig. 1). Taean is the world's second-largest coal plant, with a 6.1 GW power capacity (Nassar et al., 2021). The plant consists of ten power units with 150 m stack heights. These stacks were identified as the point sources of 13,085 tSO_2·yr^{-1} emissions by the Clean Air Policy Support System (CAPSS), the official emissions inventory. Real-time SO_2 emissions from each stack are continuously measured by an automatic monitoring system and stored in the Cleansys server. The national standard stack monitoring method (Cleansys) requires the SO_2 emission uncertainty to be <20 % relative to the daily ELV (Emission Limit Value) of 48 ppm. In recent inter-comparisons, the Cleansys SO_2 measurement uncertainties relative to ELV and percent errors relative to the reference method ranged from 3.5 to 5.4 % and 8.9– 21 % (J. Kim, personal communication, August 4, 2022), respectively. Based on this, we assumed 20 % relative errors in the Cleansys data. As this plant is located along a coastal area, stack plumes from power plants are often clearly traced over relatively clean marine background air, especially during daytime sea-breeze conditions (Abbs and Physick, 1992).

2.2. Aircraft platform

Airborne SO_2 measurements were carried out by a Beechcraft 1900D aircraft modified with four gaseous sampling and two aerosol inlets for atmospheric research. It was equipped with an airborne weather probe, AIMMS-30 (Aventech Research Inc. Barrie, Canada), consisting of an ARIM200 air data probe system and a VECTRAX inertial altitude unit system. ARIM200 is a weather sensing system that measures atmospheric
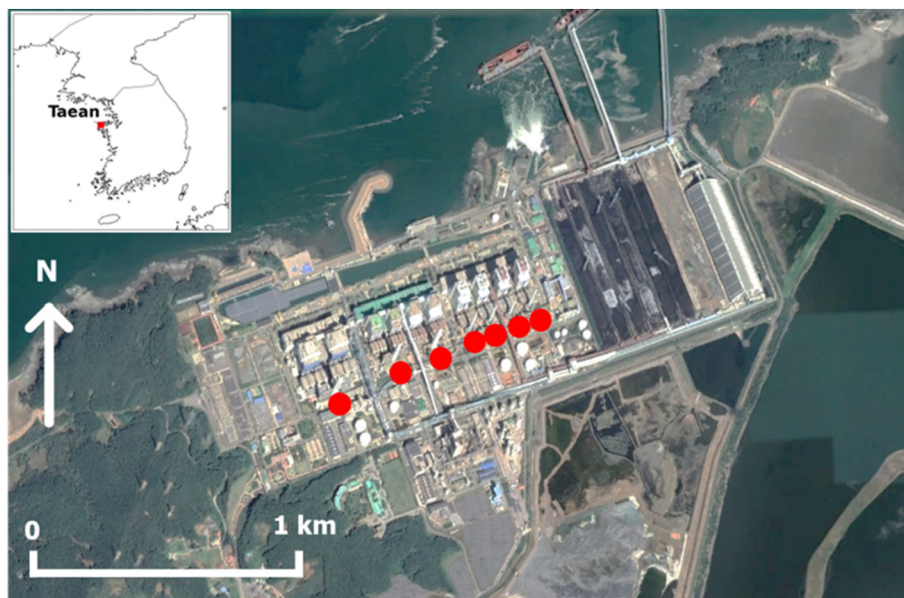
Fig. 1. Layout of the Taean power plant on the west coast of South Korea. Red dots indicate the locations of seven stacks.

pressure, temperature, relative humidity, altitude, angle of attachment, and relative wind components for the reference frame of the aircraft. In contrast, VECTRAX senses inertial acceleration, angular rates, attitude (with corresponding roll, pitch, yaw), and GPS data, including time, position, and velocity. This integrated system provides three-dimensional accurate wind components with manufacture accuracy of ± 0.4 m/s for the wind speed and ± 0.04 rad for the wind direction at aircraft positions every second, and 2 Hz measurements of SO_2 with a typical error of 12 % (Speidel et al., 2007) were obtained with a chemical ionization mass spectrometer (CIMS) using SF_6 as a reagent ion. The detailed analytical method for SO_2 using a CIMS can be found in Park et al. (2020).

2.3. Aircraft SO₂ observations

Top-down estimates of SO_2 emissions from the Taean power plant were performed during three flight observations: two on the morning and afternoon of October 21, 2019 (Flight 1 and 2), and one on the afternoon of October 27, 2020 (Flight 3). The aircraft circled the power plant at 3–8 different levels below the boundary-layer height, starting from 365 m to 914 m above sea level, to intercept the SO_2 plumes at a ~2 km radius from the stacks, close enough so that the plumes from each stack maintain their well-defined shape above the background levels and below the boundary layer height. For safety, flight restrictions prevented aircraft from flying below 350 m altitudes. Notably, the center of the stack plume can be dispersed below these minimum flight levels under strong wind conditions. The top-down airborne methods employed here are likely to significantly underestimate source emissions (a topic discussed further in the Results and Discussion).

2.4. Mass balance approach

Recent airborne studies have extensively applied mass balance techniques to derive surface ERs (Fried et al., 2020; Gordon et al., 2015; Heimburger et al., 2017; Park et al., 2020). ERs were estimated via mass balance in a cylindrical box (Eq. (1)):

$$ER \left(g \cdot s^{-1} \right) = \int_0^z \int_0^y U cos(\theta) C_i dy dz \qquad (1)$$

where *ER* is the integrated emissions rate for the horizontal (0–*y*) and vertical (0–*z*) boundary lengths (m), which are the circumference length, and height of the imaginary cylindrical box that the aircraft circularly flew across the source area, respectively. The advective flux of SO_2 was determined by integral multiplication of the observed SO_2 concentrations (C_i; ug·m^{-3}), horizontal wind velocity (U, m·s^{-1}), and angle (θ) between the wind direction and that perpendicular to the cylindrical surface (i) of the aircraft heading. Other flux-varying factors were considered insignificant, such as deposition, chemical reactions, air density changes, and turbulent flux within the box. Vertical advective flux was excluded as there were no instances of plumes passing through the top of the box throughout the study period. To apply this model, C_i, U, and θ were determined at all gridded points on the surface of the cylindrical box covering the circular flight paths across all heights. These values were extrapolated at each gridded point using kriging interpolation. Although significant gaps between the lowest flight levels and ground surface were commonly observed, no observations were made across these heights. As stack emissions sources are elevated plumes ≥ 300 m above the ground, as calculated in Table 2, zero concentrations were assumed at ground level, and linear extrapolations were made to the vertically adjacent grid cells at the lowest heights of SO_2 observation. Horizontal fluxes for all grid points at 9.5 m (z-axis) × 140 m (y-axis) resolution were projected onto a 2-D plane for each flight, and the calculated differences between the mean SO_2 influx and outflux were considered the SO_2 ER for the stack sources within the cylindrical box.

2.5. Gaussian footprint approach

The Gaussian plume model has been widely used to predict the dispersion of air pollutants from point sources (Abd El-Wahab et al., 2014; Pan et al., 2021). The concentrations at downwind distance x_i, centerline distance *y*, and height *z* from the multiple sources, with an effective height H_i, are given by Eq. (2):

$$C_{(x,y,z)} = \sum \frac{ER_i}{2\pi u \sigma_y \sigma_z} \exp\left(-\frac{y^2}{2\sigma_y^2}\right) \exp\left(-\frac{(z-H_i)^2}{2\sigma_z^2}\right) \qquad (2)$$

where ER_i is the emission rate from each point source (g·s^{-1}); *u* is the wind speed at the source level; and σ_y and σ_z are the horizontal and vertical dispersion coefficients, respectively. The two dispersion coefficients were calculated as functions of the downwind distance, along with different atmospheric stability classes. These were determined using the wind speed and solar radiation values during observation, by the Pasquill scheme

(Venkatram, 1996). This forward model predicts the spatial distribution of concentrations with a known emissions strength. The Gaussian model requires the wind directions and speeds at each stack height that we did not measure. However, the real-time observations of wind vectors at each airborne sampling location were available. Using the Gaussian footprint method, we could run it backward in time to calculate the emission sensitivity (footprint), which is the reverse source-receptor-relationship between ERs ($g \cdot s^{-1}$) from receptors and concentrations (ppbv) at sources (Seibert and Frank, 2004; Stohl et al., 2009). The SO_2 footprint fields (ppbv·g^{-1}) were calculated by running a backward Gaussian plume model using inverted winds from the given airborne sampling locations as sources. Stack parameters were subsequently used to calculate plume rises using the Briggs equation, accounting for buoyancy effects by temperature differences and momentum effects by the exiting gas velocities according to the Briggs atmospheric stability scheme (Briggs, 1969). In a conventional Gaussian plume model, the effective stack height (stack height + plume rise) is the origin of the plume advection and dispersion. Here, the individual footprint value was calculated for the effective stack height of each stack location using the reverse Gaussian method.

The SO_2 footprint values (f_{mn}) at each stack location (m), as derived from each observation position (n), were then used to estimate the emission rate (ER_m) for each stack source to match the airborne observed SO_2 concentrations (C_n) via Eq. (3):

$$
\begin{bmatrix}
f_{11} & f_{12} & f_{13} & \cdots & f_{1m} \\
f_{21} & f_{22} & f_{23} & \cdots & f_{2m} \\
\vdots & \vdots & \vdots & \cdots & \vdots \\
f_{n1} & f_{n2} & f_{n3} & \cdots & f_{mn}
\end{bmatrix}
\begin{bmatrix}
ER_1 \\
ER_2 \\
\vdots \\
ER_m
\end{bmatrix}
=
\begin{bmatrix}
c_1 \\
c_2 \\
\vdots \\
c_n
\end{bmatrix}
\tag{3}
$$

The optimal ER set minimizes the differences between the observed and calculated concentrations using linear regression or another statistical approach (Ars et al., 2017). To solve this equation, a Bayesian linear regression method was applied here. Unlike the inverse Gaussian methods using least squares, Bayesian linear regression can more readily address the uncertainties and statistical soundness of solutions due to its ability to recover the distribution of inferential solutions (Porwal and Raftery, 2022). The Bayesian linear regression package (JAGS, Just Another Gibbs Sampler) in R (*v*.4.0.5) was used to resolve this system (Su and Yajima, 2021). One major disadvantage of this approach is that reasonable prior knowledge is required to determine solutions accurately. Accordingly, CAPSS SO_2 inventory data for the Taean power plant were used as a priori data for this study. In addition, the Gaussian footprint technique assumes a stationary meteorological field and constant ER with time. A recent study revealed that the accuracy of ER-derived by mass balance method was also affected by atmospheric stability changes, wind vector variations, and emission source changes (Fathi et al., 2021). Therefore, these potential sources of uncertainty, including the airborne wind and SO_2 measurement errors, were accounted for in the mass balance model calculation. However, the uncertainties in the mass balance method were likely underestimated since we did not analyze the uncertainties by stability changes and gridding errors by interpolated data in-between the transects.

2.6. Flight times and meteorology

Three airborne SO_2 observations were made over the Taean power plants on October 21, 2019 ($n = 2$) and October 27, 2020 ($n = 1$). The average values of the meteorological variables and SO_2 concentrations observed throughout the flights are listed in Table 1. All weather parameters were acquired using the airborne weather probe, save for collecting ground wind speed data via an automatic weather station near the power station and solar radiation values obtained from the nearest fully equipped Korea Meteorological Agency (KMA) weather station. Notably, it was 3–4 °C warmer and almost two times windier in the 2019 study period compared with 2020; moreover, the observed SO_2 concentrations were 2–3 times higher in 2019. North to northeasterly winds were predominant in 2019, whereas northwesterlies were dominant in 2020. In most cases,

Table 1
Stability classes determined during the three flights and the means of their meteorological parameters at 10 m above ground level and 400 m height.

Parameters	Height	Flight 1	Flight 2	Flight 3
Stability class		B	B	A/B
Temp (°C)	Ground level	20.3	21.5	17.9
	400 m	15.2	16.3	12.8
WD (deg)	Ground level	50.7	1.2	305.0
	400 m	53.4	19.8	294.7
WS ($m \cdot s^{-1}$)	Ground level	2.7	3.0	1.9
	400 m	6.0	7.6	4.7
Solar radiation ($MJ \cdot m^{-2}$)	Ground level	2.0	1.8	1.5

sea breezes towards the landside were well characterized in the study area situated along the coastal region. Greater solar radiation and higher ground temperatures indicated intense daytime heating enhanced the local wind system in 2019. Under these fast advection conditions, lateral dispersion decreases over an equal distance. Wind speeds at 400 m were roughly two times higher than ground speeds in all cases. In contrast, values between the minimum flight altitude and ground level were extrapolated using a logarithmic scheme (Garratt, 1994). According to the Pasquill, atmospheric stability classification using wind speed and solar radiation, atmospheric stabilities on the flight days in 2019 and 2020 were categorized as classes B and A/B, respectively. These two stability classes were used to calculate the stack's effective height (due to buoyant plume rise) and the vertical and horizontal dispersion coefficients to run the Gaussian plume model. The atmospheric stability during flight 3 was initially defined as class A with the observed weather conditions. Notably, we found that the vertical dispersion coefficients (σ_z) for stability class A were so large that plumes tended to be well mixed with heights within a relatively short distance from stacks, which was not evident during the field experiment. The much-scattered plumes of flight 3 over the vertical ranges implied that the atmospheric condition was more unstable than those of previous flights with class B. The steady-state vertical dispersion coefficients from the Pasquill scheme were not adequate to simulate the instantaneous and non-steady state plume dispersion observed on a short time scale over the coastal regions between two stability classes. Park and Kim (2007) assessed the effects of various factors, including sampling time and surface roughness, on dispersion coefficients at another powerplant site in the same coastal area. We calculated the dispersion coefficients according to their proposed scheme and then estimated footprint values. There was great uncertainty in determining dispersion coefficients under unstable conditions. Later in the result section, we assessed the uncertainties ranges around the best estimate by footprint method with two different stability cases.

3. Results

3.1. Airborne observations and stack parameters

The observed SO_2 concentrations, altitudes, and wind vectors in the three flight cases, along with local flight times in Fig. 2. Flights started to circle at ~914 m over the power plant, with a radius of ~2 km, and descended to ~365 m. Airborne SO_2 measurements were performed between 10:04 and 10:13, and 14:25 and 14:33 on October 21, 2019, and between 14:22 and 14:45 on October 27, 2020, in KST. Each flight captured a few strong plumes of ≥10 ppb (Fig. 2). Flight paths were designed to track well-characterized SO_2 downwind plumes as close as possible to the power plant emissions sources, with less mixing between stacks. Northeasterly winds persisted during the two flights on October 21, 2019, flowing parallel to the stack line in the Taean power plant. Accordingly, plumes from each stack likely overlapped and merged further as they progressed. The relatively fewer peaks observed in the flights on October 21, 2019, were characteristic of plume merging. At a distance of ~2 km from the stacks, airborne measurements of SO_2 were conducted at three different altitudes in 2019. Notably, the near-field flights with three heights may
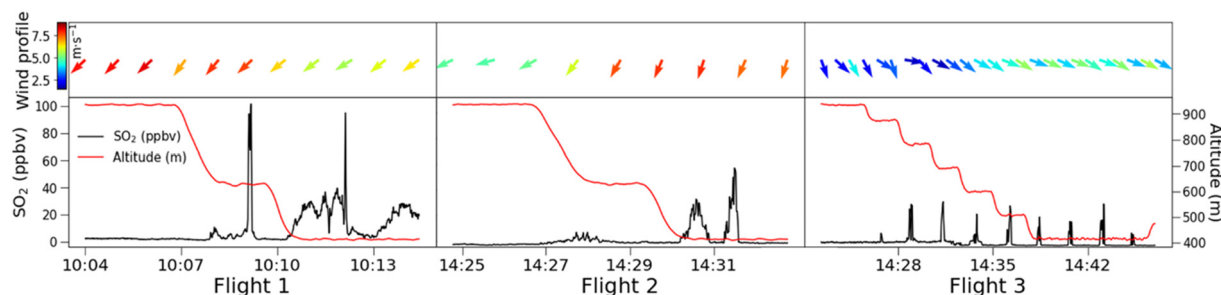
Fig. 2. Time series of SO_2 (black lines) and flight altitudes (red lines) over the three flight cases. Colored arrows indicate wind vectors with speeds.

have been too sparse to capture all plume structures from elevated stacks for the mass balance model, especially under the windy conditions observed in 2019; therefore, this number of altitudinal transects was increased to seven in 2020, as a more accurate mass balance analysis is possible at increasingly detailed vertical resolutions.

Typically, the near-field sampling scheme is suitable for tracking individual stack emissions using an inverse method if the proper links between sources and receptors can be estimated via Gaussian plume theory; however, additional parameters are required to calculate the concentration fields from stacks (i.e., meteorology and stack parameters) via observation points. Table 2 summarizes the physical and operational conditions of the seven stacks across the ten power stations in the Taean power plant. Power stations 5 + 6, 7 + 8, and 9 + 10 were paired and combined into Stacks 5, 6, and 7, respectively. All stack heights were ~150 m, with diameters ranging from 5.4 to 7.7 m. Gas exit velocities and temperatures were measured onsite by an automatic real-time stack monitoring system, where the exiting gas temperatures from all stacks were ~50 °C higher than the ambient air. As routine operational shutdowns were performed for Stack 3 on October 21, 2019, and Stack 4 on October 27, 2020, neither emission parameters nor rates were observed for these two stacks over the specific dates.

3.2. Mass balance approach

Fig. 3 shows the SO_2 concentrations depicted along 3-D flight paths for the three sampling cases. The number of altitude steps was increased to seven in 2020 to enhance the sampling resolution; thus, revealing more detailed plume structures with multiple SO_2 enhanced plume cores, further supporting the more accurate determination of power plant SO_2 emissions. SO_2 concentrations were generally low along the upwind sides over the water where no primary emissions sources were located; however, broadly elevated levels of SO_2 were distinct in the lowest altitudes along the northern to eastern sides of flight tracks, especially for the 2019 flights. Such low altitude upwind SO_2 emissions most likely originated from ground or sea level sources (e.g., ships). Although these SO_2 influxes towards the sampling columns were counted and subtracted in the mass balance model, it was clear that elevated background concentrations increased the uncertainty in the current SO_2 emissions via top-down methods. In contrast to the 2019 flights, background SO_2 concentrations along the upwind side

were low in 2020, allowing for the more accurate quantification of SO_2 patterning.

Spatially interpreted SO_2 concentrations and the observed sampling points are plotted in Fig. 4. The kriging method discussed in Section 2.4 was used to calculate SO_2 curtain plots, as plume heights and shapes were much clear in these plots. Three well-defined plume cores were discerned at elevations of 400 and 600 m on the morning of October 21, 2019 (Fig. 4a). However, by the afternoon, plume cores were only observed at the lowest height, as increased wind speeds and air temperatures rendered the plumes less buoyant and more horizontal, thereby forcing their dispersion at lower altitudes with relatively low effective heights (Table 2). It should be noted that plume cores depicted in the curtain plots did not likely represent the actual plume center due to biased interpolations from sparse transects. Although the stack plumes were not well separated when the wind directions were nearly parallel to the stack line, a few were discernable at the plume cores. On October 27, 2020, the plume heights increased to 800 m, with substantially low wind speeds and ambient temperatures. The effective heights varied significantly from 361 to 583 m on this date, generally ~100 m higher than those recorded in the previous year's flights. The significant differences in effective heights and unstable atmospheric stability (Class A/B) were likely the causes of the dispersed plume heights on the downwind side during the 2020 flight. Furthermore, horizontal separations between the plumes were more apparent as the wind blew perpendicular to the stack line on this date.

Using the mass balance equation with horizontal wind vectors and the aircraft headings interpolated at all grid points where SO_2 concentrations were measured, the net SO_2 fluxes were determined as 484 ± 142, 547 ± 155, and 690 ± 173 kg·hr^{-1} for Flights 1, 2, and 3, respectively (Table 3). SO_2 ERs for each stack were retrieved from CAPSS in the 2017 base year, the latest official emissions inventory, revealing a rate of 993 ± 288 kg·hr^{-1} for this facility. The uncertainty for SO_2 emission for the coal combustion power plants in CAPSS inventory is about 29 % (Kim and Jang, 2014). Real-time SO_2 emissions observed by the stack monitoring systems were 1969 ± 394 kg·hr^{-1}, 765 ± 153 kg·hr^{-1}, 630 ± 126 kg·hr^{-1} for Flights 1, 2, and 3, respectively. Notably, the mean of three emissions values, 1122 ± 423 kg·hr^{-1}, was similar to the CAPSS data, indicating the capacity of the CAPSS emissions data to reasonably represent overall SO_2 emissions for this power plant. Here, the emissions calculated by the mass balance method were 28–75 % lower than the Cleansys SO_2 measurements during the first

Table 2
Stack parameters and operational conditions for each stack.

| Point source	Stack height (m)	Stack effective height (m)			Stack diameter (m)	Exit gas velocity (m·s^{-1})			Exit gas temp (K)		
		#1	#2	#3		#1	#2	#3	#1	#2	#3
Stack 1	150.3	333.4	325.6	466.2	6.5	24.9	16.7	16.2	347.4	347.0	348.6
Stack 2	150.3	387.4	377.5	457.9	6.5	26.1	24.9	15.5	349.9	349.3	348.6
Stack 3	150.3	–	–	482.4	6.5	–	–	17.7	–	–	348.2
Stack 4	150.3	361.9	353.2	–	6.5	19.2	19.6	–	353.0	353.0	–
Stack 5	150.0	325.9	319.8	361.2	5.4	22.8	22.7	15.3	346.5	346.5	332.6
Stack 6	150.0	348.6	327.1	448.5	5.4	20.7	20.4	18.3	358.5	358.5	362.1
Stack 7	150.0	528.6	478.1	583.8	7.7	30.1	30.2	17.9	355.9	355.9	356.1
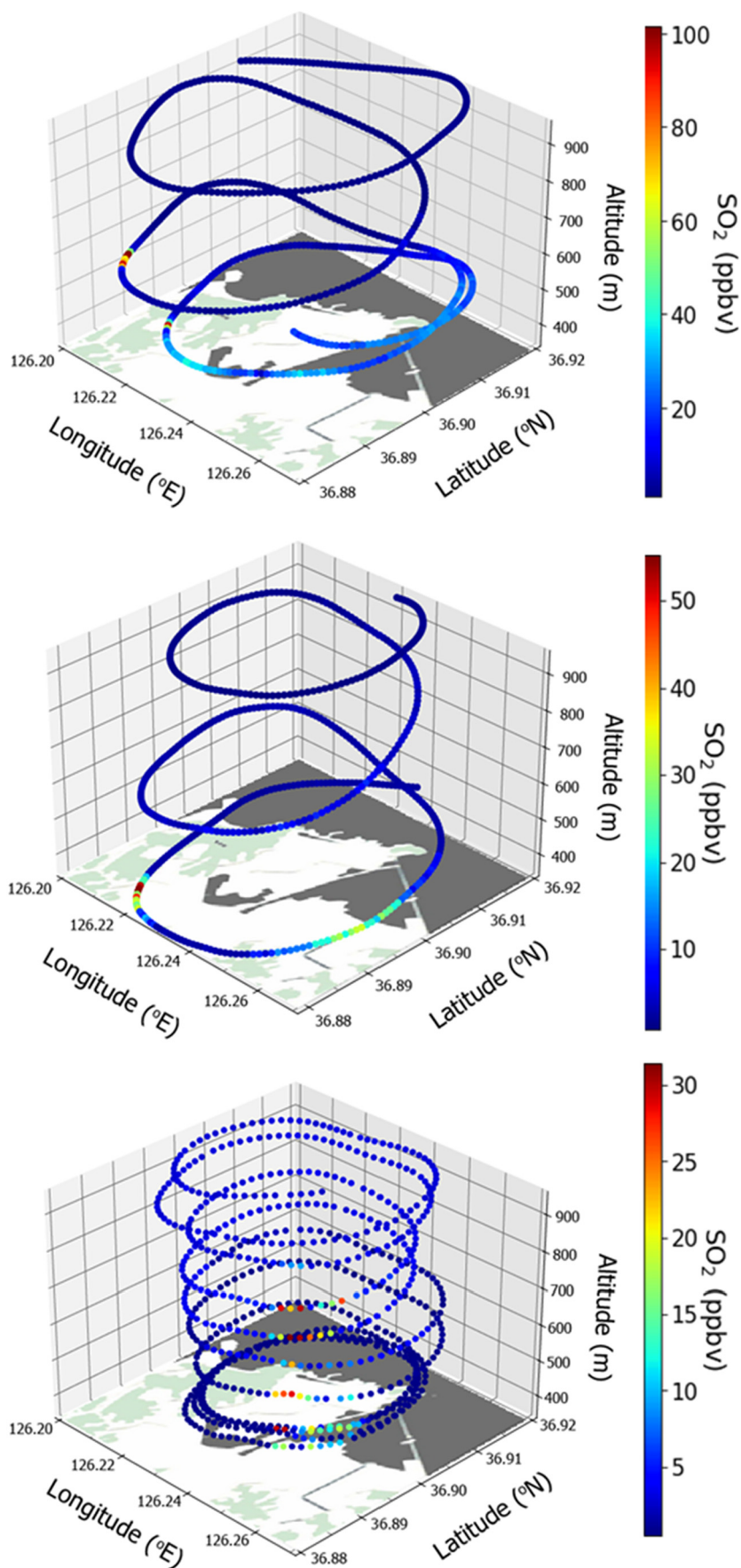
Fig. 3. SO$_2$ concentrations along the flight tracks over the Taean power plant on: (a) the morning of October 21, 2019; (b) the afternoon of October 21, 2019; and (c) October 27, 2020.
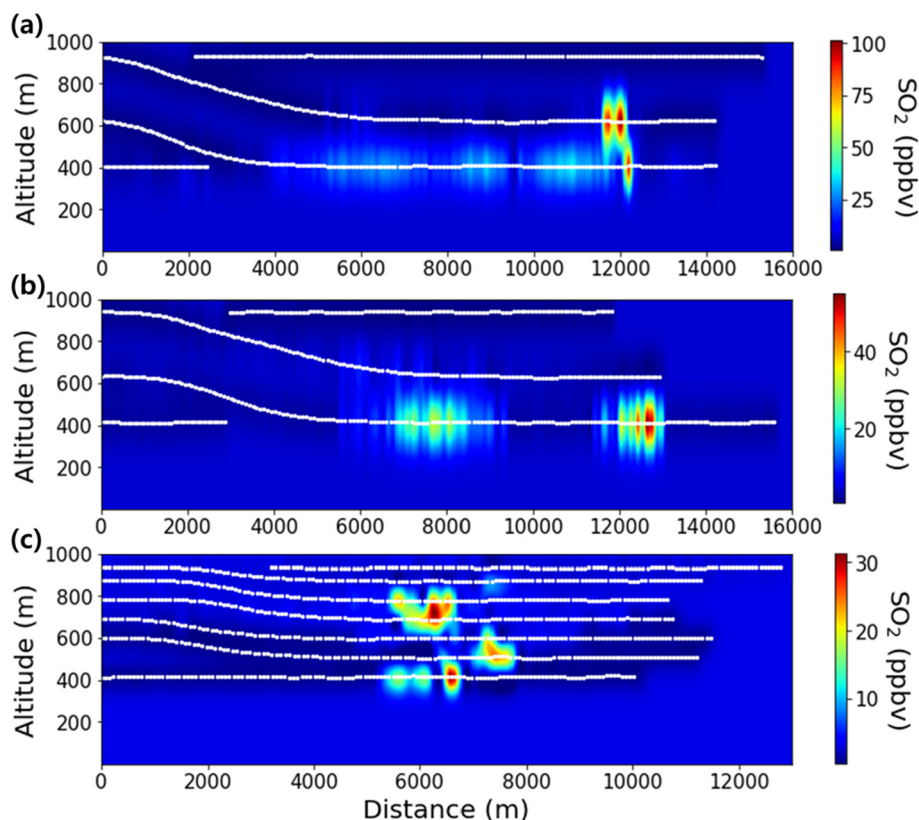
Fig. 4. SO$_2$ curtain plots on: (a) the morning of October 21, 2019; (b) afternoon of October 21, 2019; and (c) October 27, 2020. Concentrations between observation points were interpolated by kriging, and the distances were calculated from the north end of flight tracks (white lines) in a clockwise direction along the x-axis.

two flights, whereas mass balance estimates were within 10 % of the real-time values in 2020, although it underestimated CAPSS data by 30 %.

A few factors may be responsible for the observed underestimates by mass balance during Flights 1 and 2. First, it is possible that the plume cores were missed due to sub-optimally-positioned sampling transects. If the aircraft did not fly across the centers of the plume cores, the kriging interpolation would lead to a significant underestimation of the SO$_2$ concentrations. Secondly, the fast advection at higher wind speeds and more stable atmospheric conditions during Flights 1 and 2, respectively, may have also weakened the vertical plume dispersions, thereby increasing the chances of the plume passing between the widely separated transect

heights in both 2019 flights, and increasing the possibility of underestimation in the mass balance method. Lastly, an elevated SO$_2$ background on the upwind side may have resulted in lower estimates. Ideally, the upwind background concentrations do not affect the mass balance calculations, as they eventually move out of the box at the downwind side; however, the calculated influx of SO$_2$ on the upwind side was slightly more significant than its downwind outflux during Flights 1 and 2. For Flight 3, densely located sampling position heights and low background SO$_2$ concentrations both up- and downwind presented ideal conditions for the successful application of the mass balance method; consequently, the estimates derived from this approach were well-matched with real-time emissions. The

Table 3
Overall comparison of total emissions estimates implemented by the mass balance and inverse methods, with rea-time Cleansys stack emissions data and CAPSS emissions inventory from 2017 for each case flight (unit: kg·hr^{-1}).

Stacks	Flight 1			Flight 2			Flight 3			CAPSS (2017)
	Mass balance method	Foot print method	Clean sys	Mass balance method	Foot print method	Clean sys	Mass balance method	Foot print method	Clean sys	
Stack 1	–	179 ± 95	680 ± 136	–	99 ± 74	53 ± 11	–	49 ± 43	53 ± 11	46 ± 13
Stack 2	–	237 ± 98	625 ± 125	–	107 ± 73	34 ± 7	–	53 ± 44	56 ± 11	82 ± 24
Stack 3	–	188 ± 95	0	–	103 ± 73	0	–	61 ± 50	78 ± 16	71 ± 21
Stack 4	–	162 ± 91	55 ± 11	–	105 ± 573	59 ± 12	–	63 ± 52	0	85 ± 25
Stack 5	–	228 ± 104	291 ± 58	–	233 ± 101	272 ± 54	–	158 ± 81	166 ± 33	270 ± 78
Stack 6	–	118 ± 81	57 ± 11	–	120 ± 79	107 ± 21	–	84 ± 64	95 ± 19	132 ± 38
Stack 7	–	256 ± 107	262 ± 52	–	244 ± 100	241 ± 48	–	172 ± 85	184 ± 37	308 ± 89
Total	484 ± 142	1368 ± 255	1969 ± 394	547 ± 155	1010 ± 219	765 ± 153	690 ± 173	641 ± 164	630 ± 126	993 ± 288

wind speeds at stack heights are required to calculate the plume rises. As we interpolated wind speeds at stack heights using wind speeds at the nearby weather stations and about 400 m airborne measurements, some uncertainty could be expected. The calculated effective stack heights during flight 3 ranged from 361 m to 583 m above the ground (Table 2). However, the observed plume centers depicted in Fig. 4 were found between 467 m and 801 m in height, which indicated our plume rise values were underestimated by about 30 %.

3.3. Gaussian footprint approach

SO_2 footprints were calculated for all downwind sampling positions using a reverse Gaussian plume scheme. Fig. 5(a) shows an example footprint contour for a sampling position corresponding to the maximum SO_2 concentrations observed during Flight 1 (altitude, 400 m), where the seven stack locations were also marked. An advantage of the footprint method is that it can be used more efficiently to estimate the ERs over each stack source, while the mass balance method can be applied to spatially separated individual sources (Baray et al., 2018). Accordingly, footprints were calculated at the effective height for each stack (Table 2), and their frequency distributions at 0.001 s·ppbv·g^{-1} intervals are shown in Fig. 5b. During Flight 1, each stack produced some footprint values >0.1 s·ppbv·g^{-1}. These skewed data (outliers) were located on the far-right side of footprint distribution samples. A few large footprint values can dominate or distort the statistical emissions analyses. However, they were not excluded here, as they depicted accurate instantaneous measurements of more direct proximity sampling positions to stacks with less dispersion.

Fig. 5c compares the calculated ERs (posterior in Table 3) with uncertainties derived from the footprint approach with the Cleansys real-time
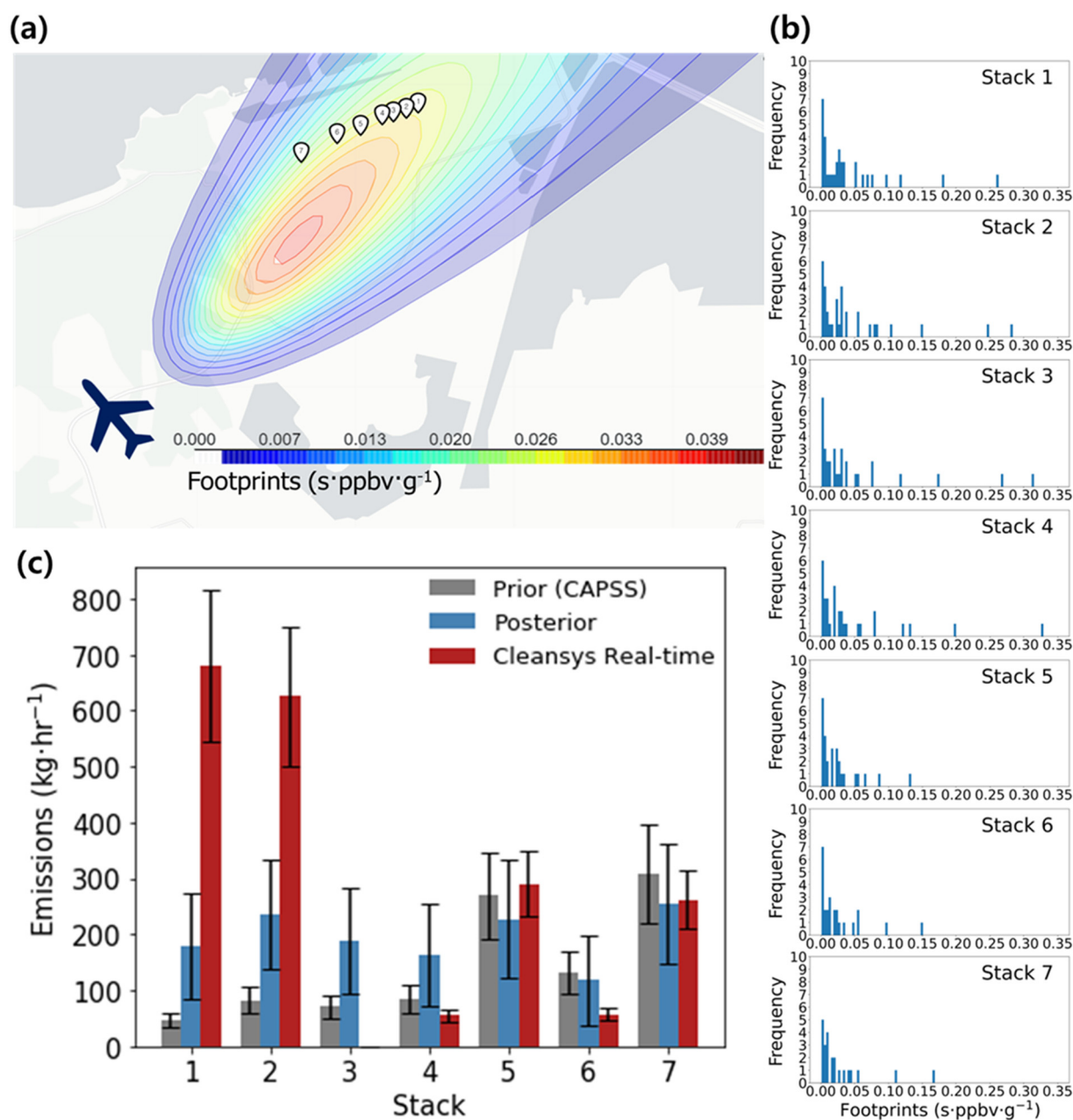

Fig. 5. (a) Calculated Gaussian footprints (s·ppb·g^{-1}) at an airborne sampling position on the morning of October 21, 2019; (b) Frequency plots showing the footprint distributions for each stack; (c) Comparison of calculated emissions rates (ERs) using the Gaussian footprint with Cleansys real-time measured ERs and a priori CAPSS inventories.

measured ERs. The SO_2 ERs allocated by the CAPSS inventory for individual stacks are also presented and were used as prior ERs for the Bayesian linear regression here. Notably, the measured and accurate SO_2 ERs of Stacks 1 and 2 were significantly higher than the CAPSS inventory (a priori) concentrations, as they were recently restarted from a routine shutdown. Compared to a priori estimates, posterior estimates significantly increased the ERs of Stacks 1 and 2; however, the reproduced values were approximately lower than half of the Cleansys measured levels, notably exceeding the calculated uncertainty range. Such a severe overestimation was also evident in Stack 3 and 4, whereas the Cleansys measured emissions well aligned with the CAPSS inventory for Stack 4. Specifically, estimates here failed to estimate zero emissions from Stack 3. Conversely, the emissions calculations were well matched in Stacks 5 and 7. The statistically significant differences between the calculated and true values were primarily attributed to inaccurate footprint calculations rather than the SO_2 measurements. For example, the position tightness of the five stacks along the footprint isopleth shown in Fig. 5a visually depicts this potential source of error. The differences between the calculated and Cleansys measured rates were improved for Stacks 6 and 7, as both agreed within an uncertainty range estimated by the Bayesian linear regression method. Notably, these stacks were positioned closest to the airborne sampling locations with more distinct footprint values.

Fig. 6 shows the footprint contour derived from the sampling position, the frequency distribution for footprints, and the estimated ER for each source stack (Fig. 6a, b, c, respectively) during Flight 2. Stacks produced more isolated footprint values as the wind shifted north and the stack line crossed the plume footprints. Further, as the wind speed was increased compared to Flight 1 at the same atmospheric stability (class B), the
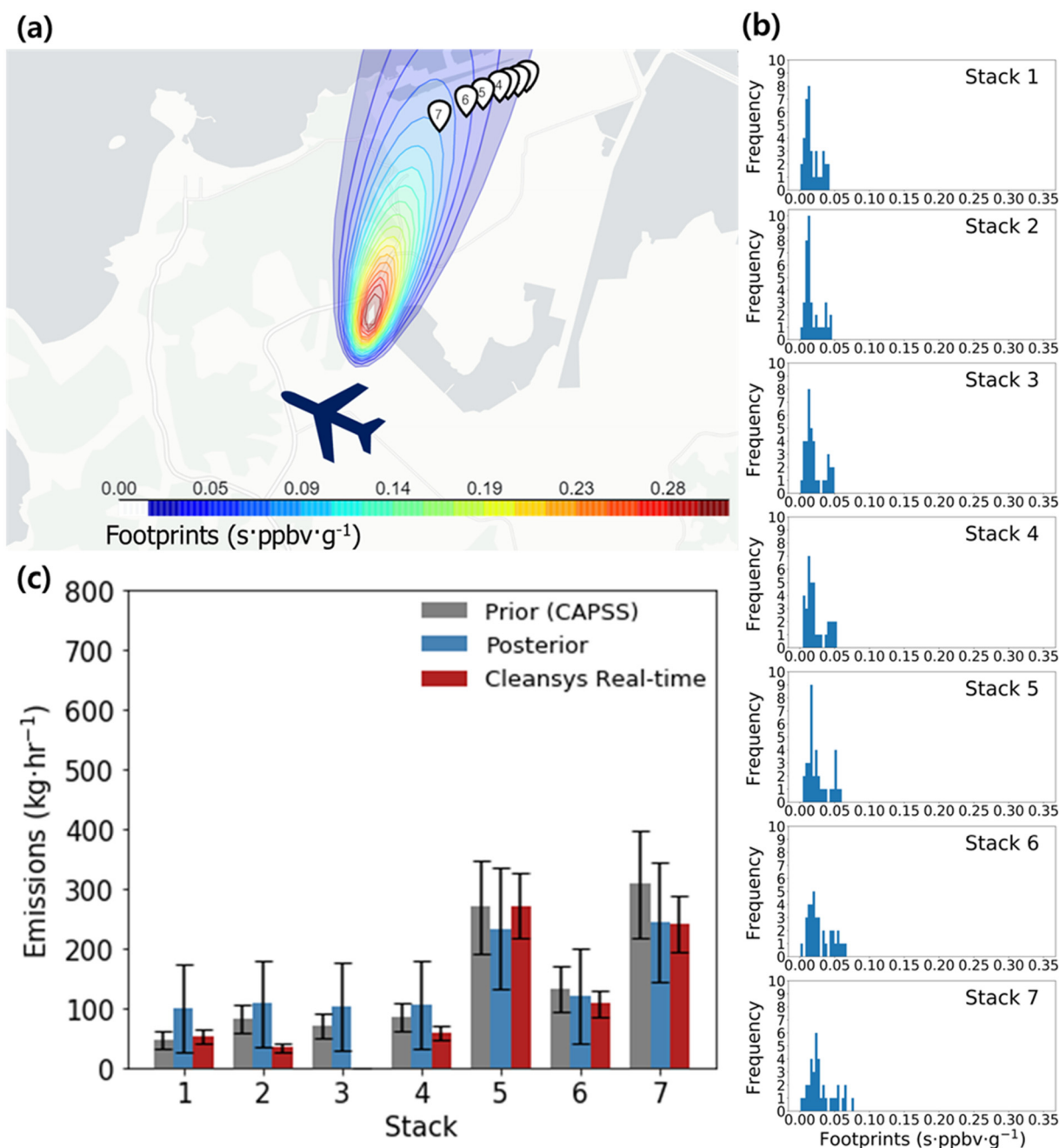

Fig. 6. (a) Calculated Gaussian footprints ($s \cdot ppb \cdot g^{-1}$) at an airborne sampling position on the afternoon of October 21, 2019; (b) Frequency plots showing the footprint distributions for each stack; (c) Comparison of calculated ERs using the Gaussian footprint with Cleansys real-time measured ERs and a priori CAPSS inventories.

footprint isopleth narrowed, and the differences in footprints between stacks increased; thus, the changing wind conditions played a significant role in optimizing the footprint approach. Similarly, the footprint frequency distributions of the stacks also indicated that Flight 2 maintained more favorable conditions for the statistical approach, as the total number of footprint values for every stack was markedly increased, thereby yielding improved statistical analyses compared to Flight 1. Furthermore, the footprint data for all stacks roughly followed a bell-shaped normal distribution, without any noticeable outliers. Consequently, relatively robust estimations of the ERs were expected in Flight 2.

During Flight 2, the overall ERs obtained using the footprint approach agreed well with the real-time rates within the calculated uncertainties, save that for Stack 3 during Flight 2 (Fig. 6c), where it appeared that the statistical method employed could not accurately account for zero emissions levels. The methods simulated reasonable ERs for Stack 5, 6, and 7 and

overestimated emissions for the other four stacks, although the estimated ERs for four stacks were within the uncertainty boundary of the estimates. Alternatively, the calculated estimates for Stack 6 and 7 performed well when compared with the measured values; however, it should be noted that the a priori CAPSS inventory values better represented the stack measured ERs in other stacks. This implies that errors were significantly inherited in the statistical footprint model, similar to Flight 1. Further, the footprint model also produced strong fits for Stacks 6 and 7, the closest upwind stacks to the airborne sampling positions.

Fig. 7 depicts the footprints and ERs during Flight 3. As the atmosphere was unstable (class A/B) with low wind speeds, the derived footprint spread most widely over the power plant. Here, the well-defined and slowly moving crosswinds perpendicular to the stack line created a distinct set of footprints. Additionally, more footprints were accumulated for all stacks resulting from the increased number of flight transects intercepting plumes
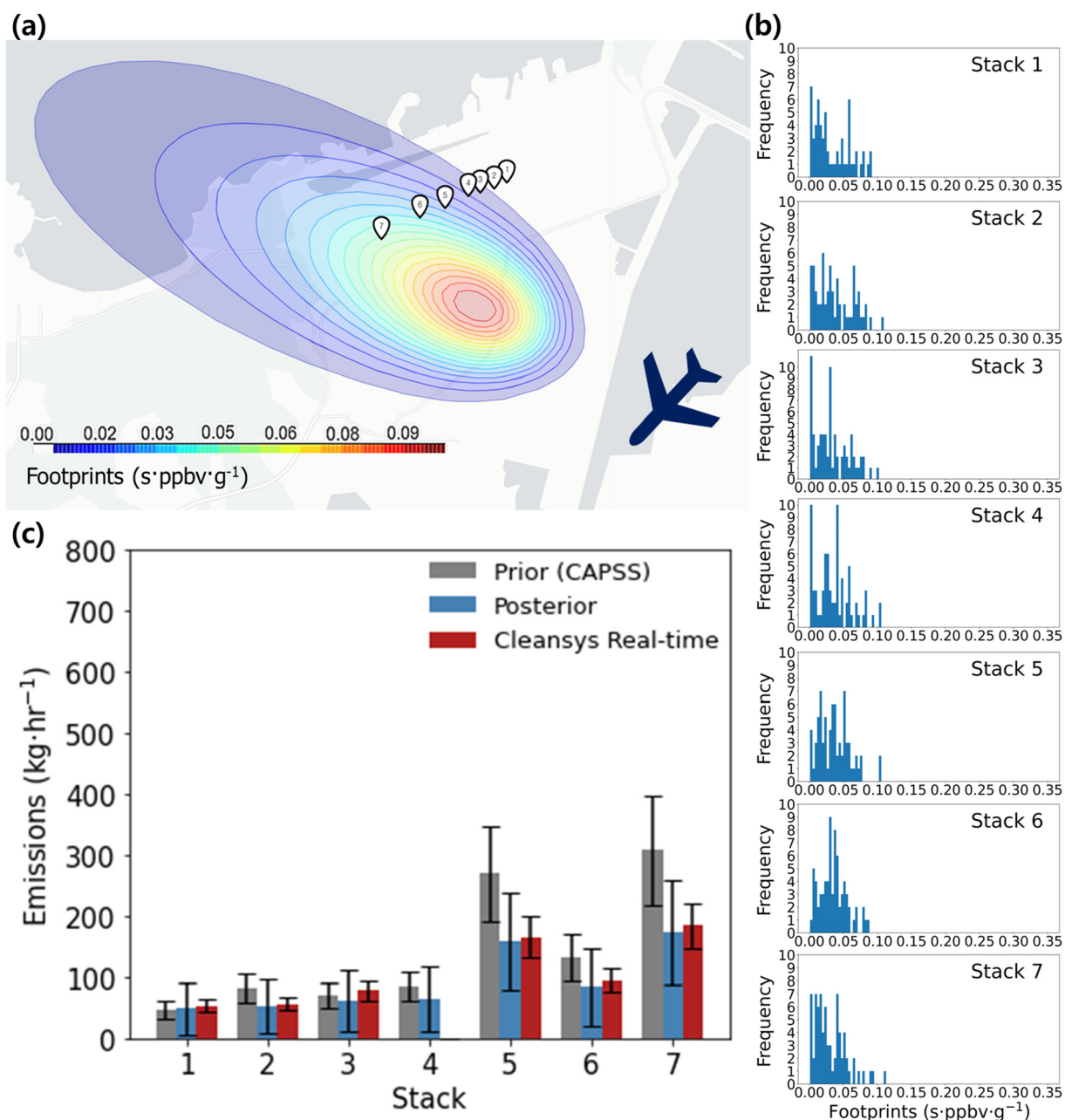

Fig. 7. (a) Calculated Gaussian footprints (s·ppb·g^{-1}) at an airborne sampling position on the afternoon of October 27, 2020; (b) Frequency plots showing the footprint distributions for each stack; (c) Comparison of calculated ERs using the Gaussian footprint with Cleansys real-time measured ERs and a priori CAPSS inventories.

during Flight 3. As a result of this increased sample size, the footprints for each stack resembled more ideal distributions.

The calculated footprint distributions during Flight 3 were typically bell-shaped with much fewer outliers than Flights 1 and 2; therefore, the reliability of emissions estimates using this statistical method was greatly enhanced by these normal distributions of calculated footprints. It was similarly found that the estimation of SO_2 ERs via footprint analysis was greatly improved by the CAPSS inventory during Flight 3. Excluding Stack 4, which was inactive during Flight 3, the combined approach of Gaussian footprints and Bayesian regressions successfully predicted the Cleansys real-time measured ERs of each stack with high accuracy, maintaining a relative difference between the calculated and real-time measured rates ranging from 5 % to 22 %. Unlike the other flights, the model results of Flight 3 retained their accuracy even for distant stacks from the downwind sampling points.

To assess the performance of the footprint method, we compared the measured SO_2 concentrations with calculated ones in Fig. 8. Most of the data over 10 ppbv of observed SO2 existed close to the 1:1 line with estimated uncertainties. However, a group of data inside the blue square box was also distinct at below 10 ppbv of SO_2, which indicated that the footprint model miscalculated the positions of plumes and overpredicted SO_2 concentrations in such cases. These mismatched data were likely made by the non-steady state characteristics of air dispersions, especially in unstable conditions, while we assumed a steady state in this study. Further improvement in the footprint method should be sought to reduce this uncertainty, mainly to reflect the non-steady state behaviors of the instantaneous plumes.

We tested how ERs for flight 3 in the footprint method were affected in the cases of no prior ER information available (Table 4). As stated in the method section, The reference run for flight 3 in Table 4 was calculated with the modified sigma values between stability classes A and B. If the initial prior ER values were set to zero (sensitivity run 1), The calculated ERs decreased significantly by approximately 62 % of the reference run. The relative differences for individual stacks between two runs ranged from 8 % to 64 %. In the result Section 3.1, we found that the observed

plume rises were approximately 50 % higher than our calculated plume values. We considered the ER variations according to the plume rise changes. In cases of plume rise increased by 50 % (sensitivity run 2), total ER got 8 % smaller than the reference run. The change in ERs by the plume rise changes was not as significant as other parameter changes. This was primarily due to the unstable atmospheric stability of flight 3 with the significant vertical dispersion coefficients. The uncertainty of calculated ER by plume rise changes would be much more significant in more stable atmospheric conditions. We have run the footprint model with two different stability conditions (A and B) to illustrate the changes in estimated ERs with varying stability. Total ER increased by 43 % and decreased by 51 % compared to the reference value, along with stability changes to A and B, respectively. This sensitivity test suggested that the availability of prior ERs and the uncertainties in dispersion coefficients in the inverse modeling method resulted in a high degree of errors, especially under very unstable conditions. Plume rise could play an additional important role in the neutral and stable atmospheric conditions.

4. Discussion

Table 3 summarizes the overall comparison of the two top-down approaches for estimating SO_2 ERs from the Taean power plant across the three flight conditions. During the first flight, both the mass balance and footprint methods underestimated SO_2 emissions compared to Cleansys values, a statistically significant difference for the mass balance method. The degree of underestimation error obtained via the mass balance method was greatly improved to 30 % during the afternoon of Flight 2 on the same day, whereas the Gaussian footprint method projected greatly overestimates. For both Flights 1 and 2, the vertical sampling resolutions were likely too sparse to capture the plume cores of each stack and reveal the maximum SO_2 concentrations. As the plume was particularly narrow, especially on this date, a higher vertical resolution with more altitudinal transects was needed to ensure that the plume cores were intercepted; thus, significant underestimates of SO_2 ERs were produced by the mass balance approach in 2019. Conversely, the Gaussian footprint method does not require plume center concentrations, as it matches any measured concentration from locations with existent source information. This is a notable advantage when detailed spatial patterns of airborne samplings are unavailable. Although the overall Gaussian footprint method produced more accurate estimates than mass balance, the individual ERs for each stack source differed significantly from the Cleansys real-time measured rates, particularly for the most distant stacks from the sampling positions (see Fig. 5 in Section 3.3). Accordingly, the inadequate number of footprints appeared to inhibit the accurate determination of stack-based ERs in the Gaussian method. Further, it was assumed that the Taean power plant was the only emissions source of the observed SO_2 concentrations; however, this was likely inaccurate during Flights 1 and 2, where notable levels of SO_2 were observed at the lowest level of the flight tracks on the upwind side. This may have contributed to the underestimation of ERs in the mass balance approach. Notably, the high background values on the upwind side did not affect the results of the footprint method, although high downwind background values may produce positively biased outcomes in either of the two cases. Thus, it is reasonable to state that the optimal performance of both methods requires either minimal background conditions or plume concentrations that are substantially higher than any background values observed if low-level fugitive emission sources exist in the vicinity of the study area.

Both requirements mentioned above were satisfied during the more detailed vertical resolution obtained and lower background SO_2 concentrations observed during Flight 3. The calculated ERs for the mass balance and Gaussian footprint methods were well matched with Cleansys real-time measured data within differences ≤10 %. As these differences were well below the estimated uncertainty, it was concluded that both methods could accurately estimate Cleansys ERs under these particular conditions. Moreover, large sets of footprints allowed for the accurate estimation of individual ERs for each stack, a notably distinct advantage of the Gaussian
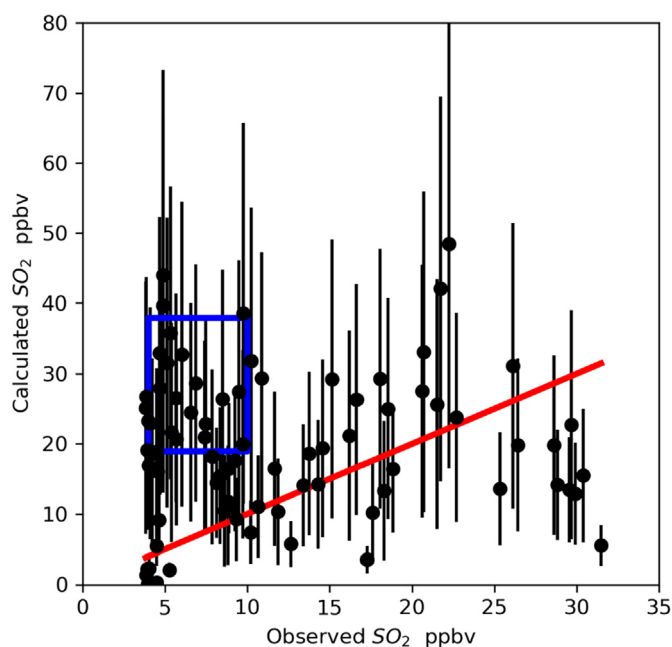

Fig. 8. Comparative plots of calculated concentrations using the Gaussian footprint method and airborne observations during flight 3. The solid red line indicates a 1:1 agreement between observed and predicted concentrations. The square regions represented data when the footprint model overpredicted SO_2 concentrations exceeding the uncertainty ranges.

Table 4
Comparison of prior and plume rise sensitivity test using the inverse method for flight 3 (unit: kg·hr^{-1}). The reference run was calculated with a priori (CAPSS) and modified dispersion coefficients for stability class A/B.

Stacks	Reference run	Sensitivity run 1	Sensitivity run 2	Sensitivity run 3	Sensitivity run 4
Stack 1	49 ± 43	41 ± 36	46 ± 39	71 ± 58	19 ± 17
Stack 2	53 ± 44	43 ± 39	49 ± 42	82 ± 62	18 ± 17
Stack 3	61 ± 50	54 ± 44	57 ± 48	87 ± 68	20 ± 17
Stack 4	63 ± 52	58 ± 47	63 ± 50	98 ± 69	21 ± 19
Stack 5	158 ± 81	70 ± 54	149 ± 82	217 ± 100	43 ± 35
Stack 6	84 ± 64	70 ± 54	78 ± 60	119 ± 76	47 ± 38
Stack 7	172 ± 85	62 ± 50	151 ± 84	240 ± 104	145 ± 64
Total	641 ± 164	398 ± 124	593 ± 160	915 ± 208	314 ± 89

Sensitivity run 1: case without known priors.
Sensitivity run 2: case of plume rise increased by 50 %.
Sensitivity run 3: case of stability A.
Sensitivity run 4: case of stability B.

method; however, the overall uncertainty in the ERs did not change significantly compared to Flight 2. It was assumed here that errors in footprint calculations and SO$_2$ measurements were constant across the entire study period, which may not be valid, particularly for footprint estimates. The accurate determination of footprints is closely dependent on the stack's effective heights and plume dispersion parameters. To this end, Mao et al. (2022) similarly indicated that the robustness of ER performances significantly decreased with an uncertain source height, whereas its accuracy was substantially reduced under uncertain dispersion parameters, as we confirmed in this study. Accordingly, the proper evaluation of footprints mandates that the uncertainties in determining the stack's effective heights and dispersion parameters are assessed extensively under different atmospheric conditions, geographical settings, and various background conditions affected by fugitive ground emissions relevant to the study area. A further drawback of the footprint method is that a steady-state assumption is required to calculate Gaussian plume dispersion. Here, flight times of 10–20 min over the Taean power plant were within the range of typical timescales for Gaussian dispersion; however, aircraft sampling can intercept only a part of an instantaneous fluctuating plume for any individual transect at a time. Alternatively, although the mass balance method does not require a steady-state plume assumption, the varying wind speeds and directions at a sampling position during a flight can significantly reduce the accuracy of the estimates (Zondlo, 2021). Overall, it was confirmed here that enhanced vertical and horizontal resolutions or multiple passes of airborne sampling points increased the accuracy of airborne top-down emissions estimates using both the mass balance and footprint methods. Furthermore, it was revealed that combining these two methods could enhance the robustness and reliability of the top-down approaches, and they can be used to verify compliance on SO$_2$ emissions regulations for significant point sources.

5. Conclusion

Via three airborne experiments conducted over the Taean power plant, South Korea, in October 2019 (Flights 1 and 2) and 2020 (Flight 3), SO$_2$ ERs were determined using mass balance and Gaussian footprint methods. Three altitudinal transects were conducted during Flights 1 and 2, whereas seven transects were conducted during Flight 3. The SO$_2$ ERs measured from the in-situ telemetry system were 1969, 765, and 631 kg·hr^{-1} for Flights 1, 2, and 3, respectively. Here, the power plant's official emissions inventory (CAPSS) represented the Cleansys SO$_2$ ERs reasonably well, except under unusual operating conditions. The mass balance method projected ERs of 484 and 547 kg·hr^{-1} for the first two flights, which were significantly lower than the Cleansys values, likely because of insufficient sampling transects to intercept the stack plumes. Also, elevated background SO$_2$ concentrations on the upwind side of the sampling flight column may have also contributed to the underestimation. The mass balance ER estimated during Flight 3 showed strong agreement with the Cleansys measured values, with a difference of <10 %. The low background SO$_2$

concentrations and the increased sampling height resolution likely allowed for the mass balance approach to more accurately estimate ERs for this date.

Overall, the Gaussian footprint analysis produced more reliable results across all cases than those derived from the mass balance method, yielding 1368; 1010; and 641 kg·hr^{-1} SO$_2$ ERs for the three flights, respectively. It was revealed that the Gaussian footprint method was less susceptible to low vertical sampling resolutions and high background concentrations on the upwind side observed during the first two flights. As the Gaussian footprint method heavily depends on reliable prior information of the source ERs, CAPSS data were applied here for Bayesian inference. Accordingly, this reliable a priori information appeared to produce more accurate estimates of SO$_2$ ERs using Gaussian footprint methods, even under less favorable conditions.

Mass balance has several distinct advantages over the Gaussian footprint method. Notably, it does not require prior information regarding the source strength and location or steady-state assumptions for estimating plume dispersion. Although it is simple and practical for use in various source applications (e.g., area sources), it is more difficult to resolve individual source strengths except for the spatially well-separated multiple sources. Alternatively, the present study demonstrated that the Gaussian footprint method successfully quantified ERs from separate point sources (i.e., power plant stacks). Here, both methods were in close agreement when satisfactory vertical resolutions were obtained and low background concentrations were observed. Thus, both implemented airborne top-down approaches were suitable for estimating the SO$_2$ ERs for significant point sources when data with sufficient spatial resolutions were obtained. Furthermore, the findings here indicate that the footprint approach and the mass balance method can add a high degree of confidence when determining the ERs from individual point sources and ensuring emissions compliance.

CRediT authorship contribution statement

Jeonghwan Kim (Visualization, Writing - review & editing).
Beom-keun Seo (Writing, Formal analysis, Visualization).
Taehyoung Lee (Investigation; Formal analysis, Methodology).
Jongho Kim (Project administration, Resources).
Saewung Kim (Data curation, Formal analysis, Methodology, Validation).
Gwi-Nam Bae (Funding acquisition, Supervision, Writing - review & editing).
Gangwoong Lee (Conceptualization, Methodology, Software, Writing - original draft, review & editing).

Funding

ICT (Grant No. 2021M3G1A1086487) and partially supported by NRF-2022R1A2C2010179.

Data availability

Data will be made available on request.

Declaration of competing interest

The authors declare that they have no known competing financial interests or personal relationships that could have appeared to influence the work reported in this paper.

Acknowledgment

The authors wish to extend their gratitude to all aircraft pilots and ground crew members of Hanseo University for supporting these research opportunities. The authors also would like to thank Editage (www.editage.co.kr) for editing and reviewing this manuscript for the English language.

References

Abbs, D.J., Physick, W.L., 1992. Sea-breeze observations and modelling: a review. Aust. Met. Mas. 41, 7–19.

Abd El-Wahab, M.M., Essa, K., Elsman, H.M., Soliman, A., Elgmmal, S.M., Wheida, A., 2014. Derivation of the Gaussian plume model in three dimensions. Mausam 65, 83–92. https://doi.org/10.54302/mausam.v65i1.892.

Ars, S., Broquet, G., Yver Kwok, C., Roustan, Y., Wu, L., Arzoumanian, E., Bousquet, P., 2017. Statistical atmospheric inversion of local gas emissions by coupling the tracer release technique and local-scale transport modelling: a test case with controlled methane emissions. Atmos. Meas. Tech. 10, 5017–5037. https://doi.org/10.5194/amt-10-5017-2017.

Baray, S., Darlington, A., Gordon, M., Hayden, K.L., Leithead, A., Li, S.-M., Liu, P.S.K., Mittermeier, R.L., Moussa, S.G., O'Brien, J., Staebler, R., Wolde, M., Worthy, D., McLaren, R., 2018. Quantification of methane sources in the Athabasca Oil Sands Region of Alberta by aircraft mass balance. Atmos. Chem. Phys. 18, 7361–7378. https://doi.org/10.5194/acp-18-7361-2018.

Briggs, G.A., 1969. Plume Rise: A Critical Survey. United States Department of Energy. Air Resources Atmospheric Turbulence and Diffusion Lab., Oak Ridge, Tenn. https://doi.org/10.2172/4743102.

Brioude, J., Kim, S.W., Angevine, W.M., Frost, G.J., Lee, S.H., McKeen, S.A., Trainer, M., Fehsenfeld, F.C., Holloway, J.S., Ryerson, T.B., Williams, E.J., Petron, G., Fast, J.D., 2011. Top-down estimate of anthropogenic emission inventories and their interannual variability in Houston using a mesoscale inverse modeling technique. J. Geophys. Res. Atmos. 116, 1–19. https://doi.org/10.1029/2011JD016215.

Cantelli, A., Leuzzi, G., Monti, P., Viotti, P., Villanova, M., Majetta, S., 2011. An inverse modeling method to identify vehicular emissions in urban complex areas. HARMO 2011 - Proceedings of the 14th International Conference on the Harmonisation Within Atmospheric Dispersion Modelling for Regulatory Purposes. Kos, Greece, pp. 617–621.

Cape, J.N., Fowler, D., Davison, A., 2003. Ecological effects of sulfur dioxide, fluorides, and minor air pollutants: recent trends and research needs. Environ. Int. 29, 201–211. https://doi.org/10.1016/S0160-4120(02)00180-0.

Carn, S.A., Krueger, A.J., Krotkov, N.A., Yang, K., Levelt, P.F., 2007. Sulfur dioxide emissions from peruvian copper smelters detected by the ozone monitoring instrument. Geophys. Res. Lett. 34. https://doi.org/10.1029/2006GL029020.

Choi, I.-H., Jo, W.-K., 2011. Application of stack emissions data from tele-monitoring systems for characterization of industrial emissions of air pollutants. Aerosol Air Qual. Res. 11, 412–418. https://doi.org/10.4209/aaqr.2011.03.0020.

Choi, S.-W., Kim, T., Lee, H.-K., Kyeong, Han, J., Lee, K.-B., Lim, E.-H., Shin, S.-H., Jin, H.-A., Cho, E., Kim, Y.-M., Yoo, C., Kim, H.-C., 2020. Analysis of the National Air Pollutant Emission Inventory (CAPSS 2016) and the major cause of change in Republic of Korea. Asian J. Atmos. Environ. 14, 422–445. https://doi.org/10.5572/ajae.2020.14.4.422.

Duncan, B.N., Prados, A.I., Lamsal, L.N., Liu, Y., Streets, D.G., Gupta, P., Hilsenrath, E., Kahn, R.A., Nielsen, J.E., Beyersdorf, A.J., Burton, S.P., Fiore, A.M., Fishman, J., Henze, D.K., Hostetler, C.A., Krotkov, N.A., Lee, P., Lin, M., Pawson, S., Pfister, G., Pickering, K.E., Pierce, R.B., Yoshida, Y., Ziemba, L.D., 2014. Satellite data of atmospheric pollution for U.S. air quality applications: examples of applications, summary of data end-user resources, answers to FAQs, and common mistakes to avoid. Atmos. Environ. 94, 647–662. https://doi.org/10.1016/j.atmosenv.2014.05.061.

Fathi, S., Gordon, M., Makar, P.A., Akingunola, A., Darlington, A., Liggio, J., Hayden, K., Li, S.-M., 2021. Evaluating the impact of storage-and-release on aircraft-based mass-balance methodology using a regional air-quality model. Atmos. Chem. Phys. 21, 15461–15491. https://doi.org/10.5194/acp-21-15461-2021.

Fried, A., Walega, J., Weibring, P., Richter, D., Simpson, I.J., Blake, D.R., Blake, N.J., Meinardi, S., Barletta, B., Hughes, S.C., 2020. Airborne formaldehyde and volatile organic compound measurements over the Daesan petrochemical complex on Korea's northwest coast during the Korea-United States Air Quality study: estimation of emission fluxes and effects on air quality. Elem. Sci. Anthr. 8.

Garratt, J.R., 1994. Appendix 3 The Atmospheric Boundary Layer. Cambridge University Press, pp. 52–56.

Gordon, M., Li, S.M., Staebler, R., Darlington, A., Hayden, K., O'Brien, J., Wolde, M., 2015. Determining air pollutant emission rates based on mass balance using airborne measurement data over the Alberta oil sands operations. Atmos. Meas. Tech. 8, 3745–3765. https://doi.org/10.5194/amt-8-3745-2015.

Heimburger, A.M.F., Harvey, R.M., Shepson, P.B., Stirm, B.H., Gore, C., Turnbull, J., Cambaliza, M.O.L., Salmon, O.E., Kerlo, A.E.M., Lavoie, T.N., Davis, K.J., Lauvaux, T., Karion, A., Sweeney, C., Brewer, W.A., Hardesty, R.M., Gurney, K.R., 2017. Assessing the optimized precision of the aircraft mass balance method for measurement of urban greenhouse gas emission rates through averaging. Elementa 5. https://doi.org/10.1525/elementa.134.

Henschel, S., Atkinson, R., Zeka, A., Le Tertre, A., Analitis, A., Katsouyanni, K., Chanel, O., Pascal, M., Forsberg, B., Medina, S., Goodman, P.G., 2012. Air pollution interventions and their impact on public health. Int. J. Public Health 57, 757–768. https://doi.org/10.1007/s00038-012-0369-6.

Hosseini, B., Stockie, J.M., 2016. Bayesian estimation of airborne fugitive emissions using a Gaussian plume model. Atmos. Environ. 141, 122–138. https://doi.org/10.1016/j.atmosenv.2016.06.046.

Kim, J., Jang, Y., 2014. Uncertainty assessment for CAPSS emission inventory by DARS. J. Korean Soc. Atmos. Environ. 30, 26–36. https://doi.org/10.5572/KOSAE.2014.30.1.026.

Kim, Y.P., Yeo, M.J., 2013. The trend of the concentrations of the criteria pollutants over Seoul. J. Korean Soc. Atmos. Environ. 29, 369–377. https://doi.org/10.5572/kosae.2013.29.4.369.

Kim, Y.P., Kim, S., Kim, J., Lee, T., 2020. Estimation of SO$_2$ emissions in large point sources at Dangjin City using airborne measurements,Part. Aerosol Res. 16, 107–117.

Lelieveld, J., Heintzenberg, J., 1992. Sulfate cooling effect on climate through in-cloud oxidation of anthropogenic SO$_2$. Science 258 (5079), 117–120. https://doi.org/10.1126/science.258.5079.117.

Lushi, E., Stockie, J.M., 2010. An inverse Gaussian plume approach for estimating atmospheric pollutant emissions from multiple point sources. Atmos. Environ. 44, 1097–1107. https://doi.org/10.1016/j.atmosenv.2009.11.039.

Mao, S., Lang, J., Chen, T., Cheng, S., Hu, F., 2022. Comparative study of source inversion under multiple atmospheric pollutant emission scenarios. Front. Environ. Sci. 10. https://10.3389/fenvs.2022.857701.

McLinden, C.A., Fioletov, V., Boersma, K.F., Krotkov, N., Sioris, C.E., Veefkind, J.P., Yang, K., 2012. Air quality over the Canadian oil sands: a first assessment using satellite observations. Geophys. Res. Lett. 39. https://doi.org/10.1029/2011GL050273.

Nassar, R., Mastrogiacomo, J.-P., Bateman-Hemphill, W., McCracken, C., MacDonald, C.G., Hill, T., O'Dell, C.W., Kiel, M., Crisp, D., 2021. Advances in quantifying power plant CO$_2$ emissions with OCO-2. Remote Sens. Environ. 264, 112579. https://doi.org/10.1016/j.rse.2021.112579.

Orellano, P., Reynoso, J., Quaranta, N., 2021. Short-term exposure to sulphur dioxide (SO$_2$) and all-cause and respiratory mortality: a systematic review and meta-analysis. Environ. Int. 150, 106434. https://doi.org/10.1016/j.envint.2021.106434.

Pan, K., Lim, M.Q., Kraft, M., Mastorakos, E., 2021. Development of a moving point source model for shipping emission dispersion modeling in EPISODE—CityChem v1.3. Geosci. Model Dev. 14, 4509–4534. https://doi.org/10.5194/gmd-14-4509-2021.

Park, O.-H., Kim, G.-S., 2007. Improvement of atmospheric dispersion model performance by pretreatment of dispersion coefficients. J. Korean Soc. Atmos. Environ. 23, 449–456. https://doi.org/10.5572/KOSAE.2007.23.4.449.

Park, M., Joo, H.S., Lee, K., Jang, M., Kim, S.D., Kim, I., Borlaza, L.J.S., Lim, H., Shin, H., Chung, K.H., Choi, Y.-H., Park, S.G., Bae, M.-S., Lee, J., Song, H., Park, K., 2018. Differential toxicities of fine particulate matters from various sources. Sci. Rep. 8, 17007. https://doi.org/10.1038/s41598-018-35398-0.

Park, J., Choi, J., Moon, K., Kim, D., Kim, H.J., Ahn, J., Lee, S., Seo, B.K., Kim, J., Park, S., Kim, S., 2020. Application of chemical ionization mass spectrometry in airborne SO2 observation on Hanseo Beechcraft 1900 D. Asian J. Atmos. Environ. 14, 413–421. https://doi.org/10.5572/ajae.2020.14.4.413.

Porwal, A., Raftery, A.E., 2022. Comparing methods for statistical inference with model uncertainty. Proc. Natl. Acad. Sci. 119, e2120737119. https://doi.org/10.1073/pnas.2120737119.

Sanchez, N.P., Saffari, A., Barczyk, S., Coleman, B.K., Naufal, Z., Rabideau, C., Pacsi, A.P., 2019. Results of three years of ambient air monitoring near a petroleum refinery in Richmond, California,USA. Atmosphere (Basel) https://doi.org/10.3390/atmos10070385.

Seibert, P., Frank, A., 2004. Source-receptor matrix calculation with a Lagrangian particle dispersion model in backward mode. Atmos. Chem. Phys. 4, 51–63. http://www.atmos-chem-phys.net/4/51/2004/.

Smith, R., 2015. Detect them before they get away: fenceline monitoring's potential to improve fugitive emissions management. Tulane Environ. Law J. 28, 433–453.

Speidel, M., Nau, R., Arnold, F., Schlager, H., Stohl, A., 2007. Sulfur dioxide measurements in the lower, middle and upper troposphere: deployment of an aircraft-based chemical ionization mass spectrometer with permanent in-flight calibration. Atmos. Environ. 41, 2427–2437. https://doi.org/10.1016/j.atmosenv.2006.07.047.

Stohl, A., Seibert, P., Arduini, J., Eckhardt, S., Fraser, P., Greally, B.R., Lunder, C., Maione, M., Mühle, J., O'Doherty, S., Prinn, R.G., Reimann, S., Saito, T., Schmidbauer, N., Simmonds, P.G., Vollmer, M.K., Weiss, R.F., Yokouchi, Y., 2009. An analytical inversion method for determining regional and global emissions of greenhouse gases: sensitivity studies and application to halocarbons. Atmos. Chem. Phys. 9, 1597–1620. https://doi.org/10.5194/acp-9-1597-2009.

Su, Y.-S., Yajima, M., 2021. Package "R2jags": Using R to Run "JAGS". http://cran.r-project.org/web/packages/R2jags.

Tang, L., Xue, X., Qu, J., Mi, Z., Bo, X., Chang, X., Wang, S., Li, S., Cui, W., Dong, G., 2020. Air pollution emissions from Chinese power plants based on the continuous emission monitoring systems network. Sci. Data 7, 325. https://doi.org/10.1038/s41597-020-00665-1.

Theys, N., De Smedt, I., van Gent, J., Danckaert, T., Wang, T., Hendrick, F., Stavrakou, T., Bauduin, S., Clarisse, L., Li, C., Krotkov, N., Yu, H., Brenot, H., Van Roozendael, M., 2015. Sulfur dioxide vertical column DOAS retrievals from the ozone monitoring instrument: global observations and comparison to ground-based and satellite data. J. Geophys. Res. Atmos. 120, 2470–2491. https://doi.org/10.1002/2014JD022657.

Vaughan, A.R., Lee, J.D., Misztal, P.K., Metzger, S., Shaw, M.D., Lewis, A.C., Purvis, R.M., Carslaw, D.C., Goldstein, A.H., Hewitt, C.N., Davison, B., Beevers, S.D., Karl, T.G., 2016. Spatially resolved flux measurements of NO_x from London suggest significantly higher emissions than predicted by inventories. Faraday Discuss. 189, 455–472. https://doi.org/10.1039/c5fd00170f.

Venkatram, A., 1996. An examination of the Pasquill–Gifford–Turner dispersion scheme. Atmos. Environ. 30, 1283–1290. https://doi.org/10.1016/1352-2310(95)00367-3.

World Health Organization, 2021. WHO global air quality guidelines: particulate matter (PM2.5 and PM10), ozone, nitrogen dioxide, sulfur dioxide and carbon monoxide. https://apps.who.int/iris/handle/10665/345329.

Zheng, X.-Y., Orellano, P., Lin, H.-L., Jiang, M., Guan, W.-J., 2021. Short-term exposure to ozone, nitrogen dioxide, and sulphur dioxide and emergency department visits and hospital admissions due to asthma: a systematic review and meta-analysis. Environ. Int. 150, 106435. https://doi.org/10.1016/j.envint.2021.106435.

Zondlo, M.A., 2021. In: Chen, W., Venables, D.S., Sigrist M.W.B.T.-A. in S.M. of the A. (Eds.), 6 - Unmanned Aerial Systems for Trace Gases. Elsevier, pp. 321–343 https://doi.org/10.1016/B978-0-12-815014-6.00007-5.